Dynamics and structure of an apolar active suspension in an annulus

Sheng Chen[1], Peng Gao[3] and Tong Gao[1,2,†]

[1]Department of Mechanical Engineering, Michigan State University, East Lansing, MI 48824, USA

[2]Department of Computational Mathematics, Science and Engineering, Michigan State University, East Lansing, MI 48824, USA

[3]Department of Modern Mechanics, University of Science and Technology of China, Hefei, Anhui 230026, PR China

We study the complex dynamics of a two-dimensional suspension comprising non-motile active particles confined in an annulus. A coarse-grained liquid crystal model is employed to describe the nematic structure evolution, and is hydrodynamically coupled with the Stokes equation to solve for the induced active flows in the annulus. For dilute suspensions, coherent structures are captured by varying the particle activity and gap width, including unidirectional circulations, travelling waves and chaotic flows. For concentrated suspensions, the internal collective dynamics features motile disclination defects and flows at finite gap widths. In particular, we observe an intriguing quasi-steady-state at certain gap widths during which $+1/2$-order defects oscillate around equilibrium positions accompanying travelling-wave flows that switch circulating directions periodically. We perform linear stability analyses to reveal the underlying physical mechanisms of pattern formation during a concatenation of instabilities.

Key words: complex fluids, liquid crystals, pattern formation

---

1. Introduction

Active matter represents a class of far-away-from-equilibrium systems comprising self-driven particles (Ramaswamy 2010; Marchetti *et al.* 2013; Shelley 2016). When immersed in a fluid, motile microstructures exert forces upon the ambient liquid, which itself acts as a coupling medium for generation of multiscale dynamics; this presents challenges in design, analysis and control of novel active materials. To take advantage of the anomalous properties (e.g. large-scale induced motion, enhanced diffusion and energy conversion), it is essential to guide active matter to perform useful mechanical work. One way of doing this is to tune the suspension concentration and the amount of chemical fuels (Sokolov *et al.* 2007; Sanchez *et al.* 2012; Henkin *et al.* 2014). Alternatively, it is possible to make use of the particle interactions, either individually or collectively, with obstacles and geometric boundaries for more direct

† Email address for correspondence: gaotong@egr.msu.edu

manipulation. By trapping active suspensions (such as pusher swimmers and Quincke rollers) within straight and curved boundaries, experimental and numerical studies have revealed stable coherent structures and flow types (Woodhouse & Goldstein 2012; Bricard *et al.* 2013; Ravnik & Yeomans 2013; Wioland *et al.* 2013; Ezhilan & Saintillan 2015; Tsang & Kanso 2016; Guillamat, Ignés-Mullol & Sagués 2016*a*; Guillamat *et al.* 2016*b*; Theillard, Alonso-Matilla & Saintillan 2017; Wu *et al.* 2017).

In this paper, we study the complex dynamics of a two-dimensional (2D) apolar active suspension confined in an annulus. The rod-like microparticles are non-motile but mobile, and are only advected by fluid flow. In the meantime, they elongate through nearly symmetric stretching or growth to exert extensile dipolar stresses on the solvent, and interact with one another through hydrodynamic coupling and steric alignment torques, which we have previously referred to as 'extensor' particles (Gao *et al.* 2017; Gao & Li 2017). Examples include bacterial cell division (Adams & Errington 2009), microtubule (MT) bundles undergoing polarity sorting driven by molecular motors (Sanchez *et al.* 2012) and tripartite Au–Pt–Au nanomotors generating surface flows due to catalytic reactions (Jewell, Wang & Malloukl 2016; Wykes *et al.* 2016). In the previous works by Gao *et al.* (2017) and Gao & Li (2017), a macroscale liquid-crystal model, i.e. '*BQ*'-tensor theory, was derived from a kinetic theory that describes the ensemble dynamics of extensors. Compared with macro models for motile suspensions (Saintillan & Shelley 2013), where the coupled evolution equations for the suspension concentration, polarity and tensorial order parameter need to be solved together, we have shown that the apolar *BQ*-tensor model naturally conserves the local concentration and the global particle numbers, and can be characterized by the evolution equation of the second-moment tensor only. Through theoretical analyses and numerical simulations for extensor suspensions both in unbounded domains and confined in circular chambers, we have demonstrated that this active fluid model, while being apolar, inherits all of the basic transitions and instabilities associated with motile suspensions, and exhibits a rich set of collective dynamics.

We examine both dilute and concentrated extensor suspensions confined in an annulus geometry. For the dilute cases, we identify emergent coherent structures that resemble those observed in 'polar' active suspensions of pusher particles (Wioland, Lushi & Goldstein 2016; Theillard *et al.* 2017) by varying the particle activity and annulus gap width. Linear stability analyses are performed to reveal the underlying physical mechanisms of a series of hydrodynamic instabilities starting from a near-isotropic state. At a finite concentration, we show that the internal collective dynamics can be effectively inhibited when confined in thin gaps; the particles rise when the gap width is large enough so that a bending instability can develop in the radial direction to generate active nematic flows. In particular, we capture an intriguing quasi-steady-state at a finite gap width featuring oscillating $+1/2$-order defects and travelling-wave flows that switch circulation directions periodically.

2. Mathematical model

We consider a collection of extensor particles suspended in a Newtonian fluid. These active particles are non-motile but can elongate or stretch near-symmetrically to produce extensional flows that effectively exert dipolar stresses upon the liquid. As shown by Gao *et al.* (2017) and Gao & Li (2017), the ensemble dynamics of extensor particles whose centre-of-mass position is located at x with an orientation p ($|p| = 1$) can be described by a probability distribution function $\Psi(x, p, t)$ through

a Smoluchowski equation. The particles exert stresses $\boldsymbol{\Sigma}$ on the liquid to drive fluid motion, which is governed by the (dimensionless) incompressible Stokes equation,

$$\nabla p - \Delta \boldsymbol{u} = \nabla \cdot \boldsymbol{\Sigma}, \tag{2.1}$$

$$\nabla \cdot \boldsymbol{u} = 0, \tag{2.2}$$

where $\boldsymbol{u}$ and p are the fluid velocity and pressure respectively. The extra stress tensor $\boldsymbol{\Sigma}$ can be written as (Saintillan & Shelley 2008; Gao *et al.* 2015*b*)

$$\boldsymbol{\Sigma} = \alpha \boldsymbol{D} + \beta \boldsymbol{S} : \boldsymbol{E} - 2\zeta\beta(\boldsymbol{D} \cdot \boldsymbol{D} - \boldsymbol{S} : \boldsymbol{D}), \tag{2.3}$$

where $\boldsymbol{E} = 1/2(\nabla \boldsymbol{u} + \nabla \boldsymbol{u}^{\mathrm{T}})$ is the rate-of-strain tensor; $\boldsymbol{D} = \int_p \boldsymbol{pp}\Psi \, \mathrm{d}\boldsymbol{p}$ and $\boldsymbol{S} = \int_p \boldsymbol{pppp}\Psi \, \mathrm{d}\boldsymbol{p}$ are the second- and fourth-moment tensors respectively, and are calculated by taking the average of $\boldsymbol{p}$ on the surface of a unit sphere. In (2.3), the first term represents a dipolar extensile stress that arises from the local extensional flows, with the dimensionless coefficient $\alpha < 0$ quantifying particle activity (Saintillan & Shelley 2008; Hohenegger & Shelley 2011). The second term is a constraining stress due to particle rigidity (Doi & Edwards 1988; Ezhilan, Shelley & Saintillan 2013), with an effective shape factor $\beta > 0$ characterizing the particle aspect ratio. The third term is due to steric interactions through a Maier–Saupe potential with a strength coefficient ζ (Maier & Saupe 1958; Ezhilan *et al.* 2013; Gao *et al.* 2015*b*). It should be noted that both the constraining and the steric interaction stresses are proportional to the effective volume fraction of the suspension, and hence cannot be neglected for concentrated suspensions (Ezhilan *et al.* 2013; Gao *et al.* 2015*b*).

The flow equation is coupled with the evolution equation of the $\boldsymbol{D}$ tensor, which is derived from the kinetic model by taking a standard moment average (Doi & Edwards 1988; Gao *et al.* 2017; Gao & Li 2017),

$$\boldsymbol{D}^{\nabla} + 2\boldsymbol{E} : \boldsymbol{S} = 4\zeta(\boldsymbol{D} \cdot \boldsymbol{D} - \boldsymbol{S} : \boldsymbol{D}) + d_T \Delta \boldsymbol{D} - 4d_R \left(\boldsymbol{D} - \frac{\boldsymbol{I}}{2} \right), \tag{2.4}$$

where $\boldsymbol{D}^{\nabla} = \partial \boldsymbol{D}/\partial t + \boldsymbol{u} \cdot \nabla \boldsymbol{D} - (\nabla \boldsymbol{u} \cdot \boldsymbol{D} + \boldsymbol{D} \cdot \nabla \boldsymbol{u}^{\mathrm{T}})$ is an upper-convected derivative, and d_R and d_T are the rotational and translational diffusion coefficients respectively. It is worthwhile to mention that in the classical Landau–de Gennes approach for liquid-crystalline fluids (de Gennes 1974), d_R and d_T are essentially the linear terms in a Landau potential and the Frank elastic constant for a nematic liquid crystal respectively. In non-dimensionalization, we assume that there are N extensor particles of length l and width b ($b/l \ll 1$) distributed in a volume V, and introduce an effective volume fraction $\nu = nbl^2$, where $n = N/V$ is the mean number density (Ezhilan *et al.* 2013; Gao *et al.* 2017; Gao & Li 2017). Then, we choose the length scale $l_c = b/\nu$, the velocity scale $|u_0|$, which represents the surface velocity due to elongation or stretching motion, and the stress scale $\mu|u_0|/l_c$. Equation (2.4) can be closed by expressing the fourth-moment tensor $\boldsymbol{S}$ in terms of $\boldsymbol{D}$ through the so-called Bingham closure (Bingham 1974; Chaubal & Leal 1998; Gao *et al.* 2017), which reconstructs a distribution function $\Psi_B(\boldsymbol{x}, \boldsymbol{p}, t)$ in terms of a traceless symmetric tensor $\boldsymbol{T}(\boldsymbol{x}, t)$, to yield

$$\Psi_B[\boldsymbol{T}] = \frac{\exp(\boldsymbol{T} : \boldsymbol{pp})}{\displaystyle\int_p \exp(\boldsymbol{T} : \boldsymbol{pp}) \, \mathrm{d}\boldsymbol{p}}. \tag{2.5}$$

We determine the tensor $\boldsymbol{T}$ numerically by solving the relation $\boldsymbol{D} = \int_p \Psi_B[\boldsymbol{T}]\boldsymbol{pp}\,\mathrm{d}\boldsymbol{p}$. Given $\boldsymbol{T}$, the fourth-moment tensor $\boldsymbol{S}$ is then approximated by $\boldsymbol{S}_B = \int_p \Psi_B[\boldsymbol{T}]\boldsymbol{pppp}\,\mathrm{d}\boldsymbol{p}$ as Ψ_B is determined by assuming that $\boldsymbol{S}$ and $\boldsymbol{D}$ are co-aligned in the principal coordinates of $\boldsymbol{D}$. We refer to the above model as the '*BQ*-tensor' model (Gao *et al.* 2017; Gao & Li 2017). In the following, we define the 2D tensor order parameter $\boldsymbol{Q}(\boldsymbol{x}, t) = \boldsymbol{D}/\phi(\boldsymbol{x}, t) - \boldsymbol{I}/2$ (here $\phi(\boldsymbol{x}, t) = \int_p \Psi\,\mathrm{d}\boldsymbol{p}$ is the concentration) whose maximal nonnegative eigenvalue λ_{max} of $\boldsymbol{Q}$ satisfies $0 \leqslant \lambda_{max} \leqslant 1/2$. We call its associated unit eigenvector the nematic director $\boldsymbol{m}$, and $0 \leqslant s = 2\lambda_{max} \leqslant 1$ the scalar order parameter.

3. Results and discussion

When simulating the confined active fluid motion, we solve the $\boldsymbol{D}$ dynamics equation (2.4) together with the incompressible Navier–Stokes equation at small Reynolds numbers ($Re = 10^{-3}$) using a mixed finite element method (Hu, Zhu & Patankar 2001; Gao & Hu 2009; Gao *et al.* 2017). At the inner ($r = R_1$) and outer ($r = R_2$) boundaries, a no-slip condition $\boldsymbol{u} = \boldsymbol{0}$ is imposed for the velocity field, and a no-flux condition $(\boldsymbol{n} \cdot \nabla)\boldsymbol{D} = \boldsymbol{0}$ is used for the second-moment tensor $\boldsymbol{D}$. It should be noted that, in this way, we do not enforce any particular alignment direction at the boundary but guarantee global particle number conservation. For all of the simulation results below, we vary α and $R_{1,2}$, and fix $d_T = d_R = 0.025$ (for both dilute and concentrated suspensions), as well as $\zeta = 0.5$, $\beta = 0.874$ (for concentrated suspensions).

3.1. *Dilute suspension*

We first examine the case of a confined dilute suspension by neglecting both the steric interaction stress ($\zeta = 0$) and the constraining stress ($\beta = 0$), and start simulations from an initially near-isotropic state. As shown in figure 1(*a–f*), where $R_1 = 1.0$ and $R_2 = 2.0$ are fixed, characteristic nematic structures and flow patterns are highlighted at different regimes of $|\alpha|$. As shown in (*a*), a unidirectional circulating flow first appears when $|\alpha|$ goes beyond a certain critical value α_{cr} (in this case, $\alpha_{cr} = -1.23$). While the nematic order is still low, as shown in (*d*), it clearly shows that particles become aligned in the azimuthal direction due to fluid shear (Saintillan & Shelley 2008; Thampi *et al.* 2015), with a stronger alignment near rigid walls. As $|\alpha|$ further increases up to 10.0 in (*b*), a circulating flow pattern still dominates but the streamlines exhibit periodic bending deformations in the radial direction to form travelling waves, leading to counterclockwise (CCW) and clockwise (CW) vortices near the inner and outer boundaries respectively. Such oscillatory patterns have also been seen in other active liquid crystal systems due to bending (or splay) deformations (Voituriez, Joanny & Prost 2005; Giomi *et al.* 2011, 2012). In (*e*), the flow-induced alignment is further enhanced to form low-order structures (blue colour). At even higher values of $|\alpha|$, the flow pattern in (*c*) becomes seemingly chaotic. The resultant nematic field exhibits a typical active liquid-crystalline phase (Sanchez *et al.* 2012; Giomi *et al.* 2013; Thampi, Golestanian & Yeomans 2014; Gao *et al.* 2015*b*; Shelley 2016), in which $\pm 1/2$ disclination defects stream around, and are constantly generated/annihilated during interactions (see *f*).

It should be noted that while our model is apolar, the observed phenomena are very similar to those reported for polar active suspensions where effects of self-swimming motions of microparticles (e.g. bacteria) are taken into account (Lushi, Wioland & Goldstein 2014; Wioland *et al.* 2016; Theillard *et al.* 2017). It is essential to recognize that the nonlinear dynamics is governed by a concatenation of hydrodynamic instabilities as α increases, and can be characterized by a series
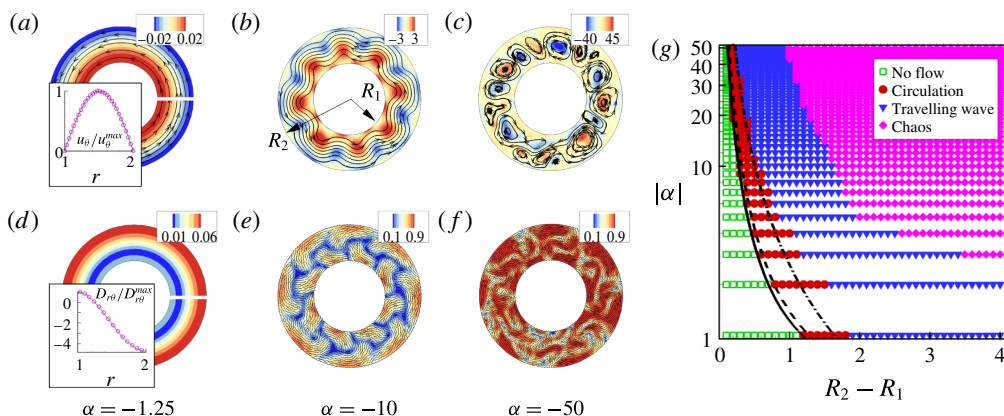
FIGURE 1. (Colour online) (*a–c*) Characteristic flow patterns (streamline overlaid on the colourmap of vorticity Ω) and (*d–f*) nematic structures (nematic director $\boldsymbol{m}$ field overlaid on the colourmap of scalar order parameter *s*) when choosing $R_1 = 1.0$ and $R_2 = 2.0$. The insets in (*a*) and (*d*) are comparisons between the analytical (solid lines) and numerical (open circles) results for normalized u_θ and $D_{r\theta}$ components taken along the white lines when $|\alpha|$ slightly goes beyond the critical value $|\alpha|_{cr} = 1.23$ for the isotropy–circulation instability. (*g*) Phase diagram of $(|\alpha|, R_2 - R_1)$ when fixing $R_1 = 1.0$. The solid and dashed lines characterize the isotropy–circulation instability in an annulus and a straight channel respectively. The dash–dotted line characterizes the circulation–travelling-wave instability in a straight channel for sharply aligned rods by neglecting the rotational diffusion.

of instabilities including isotropy to circulation, circulation to travelling wave and travelling wave to chaos. An overview of the instabilities is presented in a phase diagram plotted in the $(|\alpha|, R_2 - R_1)$ plane in (*g*), where R_1 is fixed to be 1.0. Furthermore, the marginal stability curve that delineates the isotropy–circulation instability can be calculated analytically in the polar coordinates. To do this, we perturb the near-isotropic solutions as $\boldsymbol{D} = \boldsymbol{I}/2 + \epsilon \boldsymbol{D}'(r)$ and $\boldsymbol{u} = \epsilon \boldsymbol{u}'(r)$ ($\epsilon \ll 1$) by assuming azimuthal symmetry. Following the procedure of Woodhouse & Goldstein (2012), we examine an initially exponential growth $\partial \boldsymbol{D}'/\partial t = \kappa \boldsymbol{D}'$ with the growth factor $\kappa \geqslant 0$. After some algebra, we find $D'_{rr} = D'_{\theta\theta} = 0$, and the hydrodynamic instability arises from the following coupled linearized equations for u'_θ and $D'_{r\theta}$:

$$\frac{\partial u'_\theta}{\partial r} - \frac{u'_\theta}{r} + \alpha D'_{r\theta} = \frac{A_0}{2r^2}, \tag{3.1}$$

$$r^2 \frac{\partial^2 D'_{r\theta}}{\partial r^2} + r \frac{\partial D'_{r\theta}}{\partial r} + (\gamma r^2 - 4) D'_{r\theta} = -\frac{A_0}{4d_T}, \tag{3.2}$$

where $\gamma = -((16d_R + 4\kappa + \alpha)/4d_T)$. We are able to seek the solutions $D'_{r\theta} = -(A_0/4\gamma d_T r^2) + A_1(\partial J_2(\sqrt{\gamma}r)/\partial r) + A_2(\partial N_2(\sqrt{\gamma}r)/\partial r)$ and $u'_\theta = -(A_0/2r)(1 + \alpha/4\gamma d_T) + (2A_1/\sqrt{\gamma})J_1(\sqrt{\gamma}r) + (2A_2/\sqrt{\gamma})N_1(\sqrt{\gamma}r) + A_3 r$, where J_j and N_j are respectively Bessel functions of the first and second kinds, with coefficients A_j to be determined. By applying boundary conditions $\partial D'_{r\theta}/\partial r = 0$ and $u'_\theta = 0$ on the two walls, we then solve the eigenvalues of γ numerically at $\kappa = 0$ (solid line in *g*), as well as the velocity and $\boldsymbol{D}$ field (insets in *a,d*), which, again, confirm our simulation results.

Next, we reveal the nature of the hydrodynamic instabilities and gain physical insight into the formation of the observed coherent structures in figure 1. As shown below, while analytical approaches are feasible for the isotropy–circulation and circulation–travelling-wave transitions, the travelling-wave–chaos instability is highly nonlinear and hence can only be explored numerically. Here, we avoid tedious mathematical manipulations in the polar coordinates to simplify our analysis by considering confinement in a straight periodic channel (i.e. in the limit $R_{1,2} \to \infty$), where very similar collective dynamics and hydrodynamic instabilities are observed (Theillard *et al.* 2017). For the two cases considered, we employ a homogeneous base-state solution of $\boldsymbol{D}_0$ without background flow (i.e. $\boldsymbol{u}_0 = \boldsymbol{0}$, $p_0 = 0$), and introduce perturbations $(\boldsymbol{D}', \boldsymbol{u}', p')$ to yield the following linearized equations:

$$\frac{\partial \boldsymbol{D}'}{\partial t} - (\nabla \boldsymbol{u}') \cdot \boldsymbol{D}_0 - \boldsymbol{D}_0 \cdot (\nabla \boldsymbol{u}'^{\mathrm{T}}) + 2\boldsymbol{E}' : \boldsymbol{S}_0 = d_T \nabla^2 \boldsymbol{D}' - 4d_R \boldsymbol{D}', \tag{3.3}$$

$$\nabla p' - \Delta \boldsymbol{u}' = \nabla \cdot (\alpha \boldsymbol{D}'), \tag{3.4}$$

$$\nabla \cdot \boldsymbol{u}' = 0, \tag{3.5}$$

with boundary conditions $\partial \boldsymbol{D}'/\partial y = 0$ and $\boldsymbol{u}' = 0$ on the upper $(y = h)$ and bottom $(y = -h)$ walls. (It should be noted here that $D'_{11} + D'_{22} = 0$.) We then take a Fourier transform in the x direction of all perturbed quantities $\boldsymbol{f}'$ such that $\boldsymbol{f}'(x, y) = \tilde{\boldsymbol{f}}(k, y) \exp(\mathrm{i}kx + \sigma t)$, where $\tilde{\boldsymbol{f}}$ is the amplitude function, k is the wavenumber and σ is the complex-valued growth rate.

Case 1: isotropy–circulation instability. In this case, the instability grows from an initially isotropic state, i.e. $\boldsymbol{D}_0 = \boldsymbol{I}/2$. The linearized equations in (3.3) and (3.5) become

$$(\delta^{(2)} - k^2)^2 \tilde{v} + 2\alpha k^2 \delta \tilde{D}_{11} - \mathrm{i}k\alpha(\delta^{(2)} + k^2)\tilde{D}_{12} = 0, \tag{3.6}$$

$$2d_T(\delta^{(2)} - \omega)\tilde{D}_{11} - \delta \tilde{v} = 0, \tag{3.7}$$

$$4d_T k(\delta^{(2)} - \omega)\tilde{D}_{12} + \mathrm{i}(\delta^{(2)} + k^2)\tilde{v} = 0, \tag{3.8}$$

where $\delta^{(n)} = \mathrm{d}^n/\mathrm{d}y^n$ represents the nth derivative of y, and $\omega = (\sigma + 4d_R)/d_T + k^2$. We find that the general solution of the above equations has the vector form

$$\begin{aligned}
(\tilde{D}_{11}, \tilde{D}_{12}, \tilde{v}) = \ &(B_1 \boldsymbol{F}_1 + B_2 \boldsymbol{F}_2)\mathrm{e}^{ky} + (B_3 \boldsymbol{F}_3 + B_4 \boldsymbol{F}_4)\mathrm{e}^{-ky} \\
&+ B_5 \boldsymbol{F}_5 \mathrm{e}^{\sqrt{\omega}y} + B_6 \boldsymbol{F}_6 \mathrm{e}^{-\sqrt{\omega}y} + B_7 \boldsymbol{F}_7 \mathrm{e}^{\mathrm{i}\sqrt{-\chi}y} + B_8 \boldsymbol{F}_8 \mathrm{e}^{-\mathrm{i}\sqrt{-\chi}y},
\end{aligned} \tag{3.9}$$

where $\chi = \omega + \alpha/4d_T$, and $\boldsymbol{F}_j$ can be written as

$$\boldsymbol{F}_1 = \{\mathrm{i}k, k, 2\mathrm{i}d_T(k^2 - \omega)\}, \quad \boldsymbol{F}_2 = \{\mathrm{i}k^2 y, k^2 y, 2\mathrm{i}d_T[k(k^2 - \omega)y + k^2 + \omega]\}, \tag{3.10a,b}$$

$$\boldsymbol{F}_3 = \{-\mathrm{i}k, k, 2\mathrm{i}d_T(k^2 - \omega)\}, \quad \boldsymbol{F}_4 = \{-\mathrm{i}k^2 y, k^2 y, 2\mathrm{i}d_T[k(k^2 - \omega)y - k^2 - \omega]\}, \tag{3.11a,b}$$

$$\boldsymbol{F}_5 = \{\mathrm{i}(k^2 + \omega), 2\sqrt{\omega}k, 0\}, \quad \boldsymbol{F}_6 = \{-\mathrm{i}(k^2 + \omega), 2\sqrt{\omega}k, 0\}, \tag{3.12a,b}$$

$$\boldsymbol{F}_7 = \{2k\sqrt{-\chi}, -\chi - k^2, -\mathrm{i}\alpha k\}, \quad \boldsymbol{F}_8 = \{-2k\sqrt{-\chi}, -\chi - k^2, -\mathrm{i}\alpha k\}. \tag{3.13a,b}$$

By implementing the eight boundary conditions $\delta \tilde{D}_{11} = \delta \tilde{D}_{12} = \delta \tilde{v} = \tilde{v} = 0$ at $y = \pm h$, we obtain a linear system for B_j. The existence of non-trivial solutions gives ω and hence σ. On the other hand, we find that the long-wave solution has to be solved separately due to a singularity at $k = 0$. By making use of the fact that the solution is unidirectional, we are able to obtain the equilibrium solution,
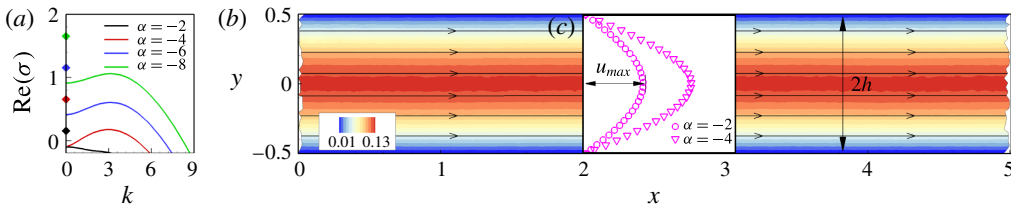
FIGURE 2. (Colour online) (*a*) The growth rate $\mathrm{Re}(\sigma)$ for the long-wave (diamonds) and finite-wavelength (lines) instabilities as a function of the wavenumber k for isotropy–circulation instabilities in a periodic straight channel when choosing $h = 0.5$, $d_T = d_R = 0.025$. (*b*) Streamlines overlaid on the colourmap of the u velocity component at $\alpha = -4.0$. (*c*) Velocity profiles at $\alpha = -2.0$ ($u_{max} = 0.07$) and $\alpha = -4.0$ ($u_{max} = 0.13$) respectively.

$(\tilde{D}_{11}, \tilde{D}_{12}, \tilde{v}) = (0, \, \sin \, (\sqrt{(\alpha + 4\sigma + 16d_R)/4d_T}y), \, \cos \, (\sqrt{(\alpha + 4\sigma + 16d_R)/4d_T}y))$, which yields the growth rate

$$\sigma = -\frac{\alpha}{4} - \left(\frac{\pi}{2h}\right)^2 d_T - 4d_R \quad \text{at } k = 0. \tag{3.14}$$

As shown by the comparisons in figure 2(*a*), we find that the real parts of the growth rates of the long-wave modes (diamond symbols) are always larger than those of the corresponding finite-wavelength ones (solid lines), and hence dominate the instability. Moreover, (3.14) suggests a marginal stability condition, $|\alpha| > 4(\pi/2h)^2 d_T + 16d_R$, which recovers the theoretical predictions for unbounded suspensions in the limit $h \to \infty$ (Gao *et al.* 2015*b*). When making connections to the annulus geometry by replacing the gap width $2h$ by $R_2 - R_1$, we find that the marginal instability curve in figure 1(*g*) can be accurately fitted as a function of the form $K(R_2 - R_1)^{-2}d_T + 16d_R$ but with a different constant K due to curved geometries (in this case, $K \approx 28.7$). It is apparent that the prediction in the straight periodic channel (dashed line in figure 1*g*) agrees well with that of the curved annulus, suggesting that (3.14) in fact provides a reasonable estimate of the time scale of the isotropy–circulation instability under a general parallel confinement.

Case 2: circulation–travelling-wave instability. It needs to kept in mind that the circulation–travelling-wave instability is in fact a secondary instability developed from a shear-induced aligned state whose analytical form, however, is lacking. Nevertheless, we consider a reduced model where all of the extensor particles are initially aligned in the x direction, and neglect the rotational diffusion by choosing $d_R = 0$ (Gao *et al.* 2017). For such a 'sharply aligned' configuration, the homogeneous base-state solution is simply $\mathbf{D}_0 = \mathrm{diag}\{1, 0\}$. After some algebra, we are able to eliminate several unknown variables, and show that the hydrodynamic instability is determined by the following sixth-order ordinary differential equation for the off-diagonal component $\tilde{D}_{12}$:

$$\left(\delta^{(6)} - k^2 \left(\frac{\sigma}{d_T k^2} + 3\right) \delta^{(4)} + k^4 \left(\frac{2\sigma - \alpha}{d_T k^2} + 3\right) \delta^{(2)} - k^6 \left(\frac{\sigma + \alpha}{d_T k^2} + 1\right)\right) \tilde{D}_{12} = 0, \tag{3.15}$$

which admits the general solution $\tilde{D}_{12} = \sum_{j=1}^{6} C_j \exp(\lambda_j y)$. The eigenvalues λ_j and hence the growth rate σ are then solved numerically by applying the converted
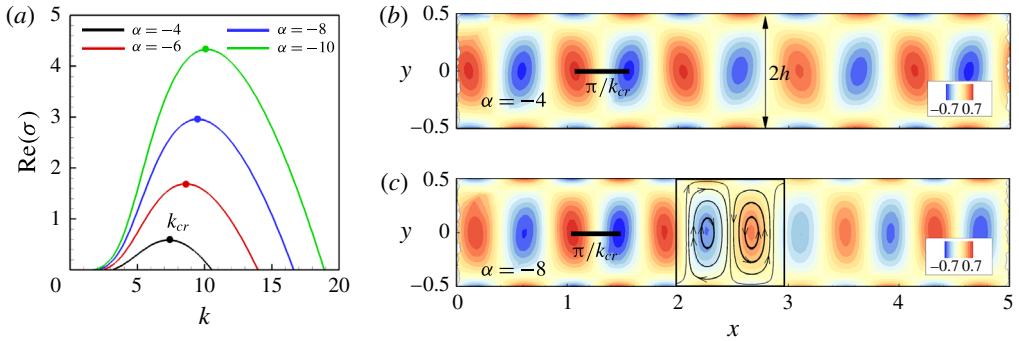
FIGURE 3. (Colour online) (*a*) The growth rate Re(σ) as a function of the wavenumber k for bending instabilities of the sharply aligned extensors when confined in a periodic straight channel when choosing $h = 0.5$, $d_R = 0$ and $d_T = 0.025$. The maximum growth rates at the critical wavenumbers k_{cr} are marked by solid circles. (*b,c*) The vorticity field Ω as the bending instability starts to grow at $\alpha = -4.0$ and $\alpha = -8.0$ respectively. The solid black scales represent the length scales π/k_{cr} that match the separation distance between the neighbouring vortices.

boundary conditions $(\sigma + d_T k^2)\tilde{D}_{12} - d_T \delta^{(2)}\tilde{D}_{12} = 0$ and $\delta\tilde{D}_{12} = \delta^{(3)}\tilde{D}_{12} = 0$ at $y = \pm h$, and seeking non-trivial solutions. The real parts of the growth rates as a function of k are plotted in figure 3(*a*) at different values of α, showing that the maximum growth rates occur at finite critical wavenumbers $k_{cr} > 0$. In (*b,c*), we set up the corresponding numerical simulations with the same initial conditions, and highlight the snapshots of the vorticity field $\Omega = \partial u/\partial y - \partial v/\partial x$. The simulation results show the generation of fluid jets that are perpendicular to the particle alignment direction due to the nematic bending instability, which leads to uniformly spaced vortices of alternating signs. The separation distance between neighbouring vortex pairs can be accurately measured by the characteristic length scale π/k_{cr}.

While the above analysis is for a reduced model by assuming particle alignment in the x direction without background flow, it reveals the finite-wavelength nature of the bending instability, and provides quantitative measurements for the intrinsic time and length scales selected by the parallel confinement. Similarly to case 1, the predicted circulation–travelling-wave borderline (dash–dotted line in (*g*)) in the straight channel indeed agrees with the simulation results for the annulus geometry, especially in the regime of high $|\alpha|$ and small $R_2 - R_1$, where particles are strongly aligned and hence close to the sharp-alignment approximation. Beyond the travelling-wave regime, the transition towards chaotic flows is highly nonlinear, and can only be determined by numerical simulations.

3.2. *Concentrated suspension*

In this section, we examine the nonlinear dynamics of concentrated suspensions where both β and ζ are non-zero. A mean-field torque is introduced to govern the rotational dynamics of extensor particles in the kinetic model through a Maier–Saupe steric potential (Maier & Saupe 1958). As shown by Gao *et al.* (2015*a,b*, 2017), for rod-like particles, the resultant enhanced steric interactions spontaneously drive the system away from an initially isotropic state to form a nematically aligned state when $\zeta > 4d_R$.

Compared with the dilute cases where isotropy is the only admissible equilibrium state, we have obtained the steady-state solutions of ***D*** without flows at relatively small
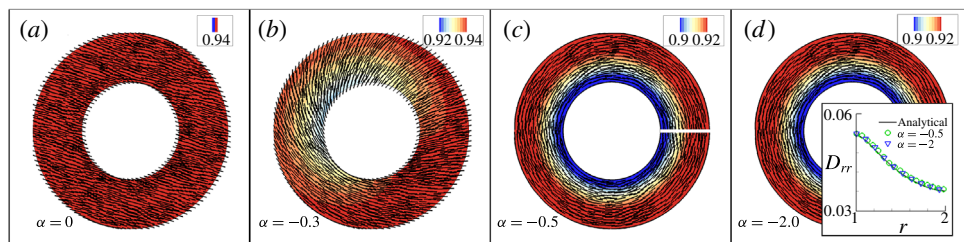
FIGURE 4. (Colour online) Equilibrium solutions of nematically aligned states at different values of α when choosing $R_1 = 1.0$ and $R_2 = 2.0$; the nematic director field is overlaid on the colourmap of s. Inset in (d): comparisons between the analytical (solid line) and numerical (open symbols) results at $\alpha = -0.5, -2.0$ for the D_{rr} component. The numerical data are taken along the white line marked in (c).

values of $|\alpha|$, which exhibit much more complicated nematic configurations, as shown in figure 4. For passive particles, when choosing $\alpha = 0$, figure 4(a) reveals that the system quickly relaxes to a homogeneous nematic state where the equilibrium solution satisfies a 2D distribution of Bingham form (Gao *et al.* 2015b, 2017; Gao & Li 2017),

$$\Psi_B(\phi) = \frac{\exp[\delta(\xi)\cos(2\phi)]}{\displaystyle\int_0^{2\pi} d\phi' \exp[\delta(\xi)\cos(2\phi')]}, \tag{3.16}$$

where ϕ is the rod orientation angle and δ is a function of the coefficient $\xi = 2\zeta/d_R$. Therefore, the degree of alignment is in fact determined by the ratio between ζ and d_R. As α increases, it is seen that the nematic field lines in figure 4(b) become distorted to spiral outwards to the annulus boundaries, reminiscent of the defect structures of active nematics when confined in a circular disk (Woodhouse & Goldstein 2012; Gao *et al.* 2017). As $|\alpha|$ approximately goes beyond 0.5, the nematic structures in figure 4(c,d) switch to become azimuthal-symmetric and independent of the values of α, which can be solved analytically by setting the right-hand side of (2.5) to be zero and then seeking the steady-state solution of $\boldsymbol{D}$ as a function of r only. The observed variations in the equilibrium nematic states can be illustrated by examining the system transient dynamics that evolves from near-isotropy. One interesting example is shown in figure 5 when choosing $\alpha = -2.0$. An isotropy–circulation instability first occurs in figure 5(a) to reorient particles, due to the combined effect of the circulating flow and the Maier–Saupe steric interactions. However, in this case, the confinement effect in the thin gap is so strong that it suppresses the bending deformation occurring in the radial direction. As a result, the induced circulating flow gradually diminishes and the system eventually relaxes to an axisymmetric equilibrium state where all particles are approximately aligned in the azimuthal direction; see the insets in figure 5(b–d).

Increase of the gap width relaxes the confinement effect to facilitate the active flow generation through the bending instability, which can be similarly explained by the analysis in the dilute cases above. As shown in figure 6, the system long-time dynamics clearly exhibits an isotropy–circulation (b,f) and then a circulation–travelling-wave (c,g) instability. Compared with the stable structures observed in the dilute cases, the structure formation and evolution in concentrated suspensions are much more complicated. In (c), it is shown that the active flows bend the streamlines to form travelling waves, leading to six evenly spaced 'incipient
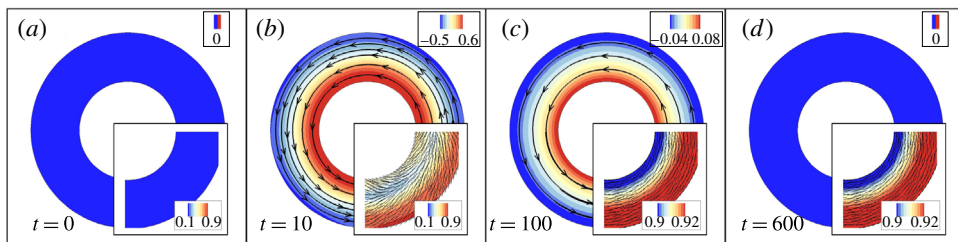
FIGURE 5. (Colour online) Evolution of the flow patterns for a concentrated extensor suspension when choosing $\alpha = -2.0$, $R_1 = 1.0$ and $R_2 = 2.0$. Insets: the nematic director field overlaid on the colourmap of s.
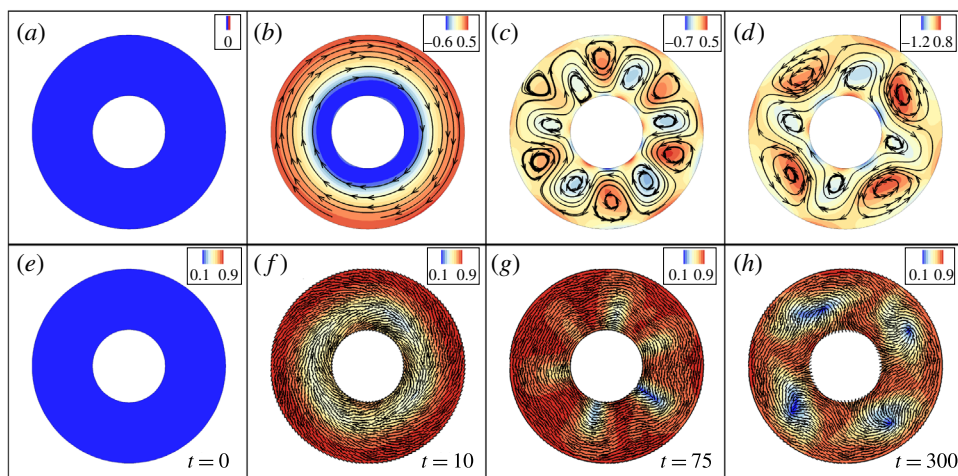

FIGURE 6. (Colour online) (a–d) Flow patterns (streamline overlaid on the colourmap of Ω) and (e–h) nematic structures (nematic director field overlaid on the colourmap of s) that characterize the long-time dynamics of a confined extensor suspension when choosing $\alpha = -2.0$, $R_1 = 0.75$ and $R_2 = 2.0$.

cracks' growing from the inner wall into the bulk regime shown in (g). Disclination defects of charge $\pm 1/2$ are seen to be born along these cracks, move around and undergo nucleation/annihilation when interacting with each other as well as with rigid boundaries. Interestingly, the system gradually approaches a quasi-steady-state where four $+1/2$ defects oscillate around their equilibrium positions; see (h). The flow field remains travelling-wave-like but also periodically switches directions; see (d). The entire history of the complex dynamics is shown in the supplementary movie S1 (available at https://doi.org/10.1017/jfm.2017.759).

As shown in figure 7, a close look at the short-time dynamics of oscillating $+1/2$ defects and the accompanying swirling flow reveals the subtle interplay among the nematic structure variation, the active flow generation and their interactions with the curved walls. The swirling flow drives the upward movement of the $+1/2$ disclination defect and, in the mean time, induces an opposite bending deformation nearby to form an incipient crack. As shown in (f,g), the crack 'head' keeps moving downward to become a $+1/2$ defect (see (h)), while its 'tail' gradually merges with
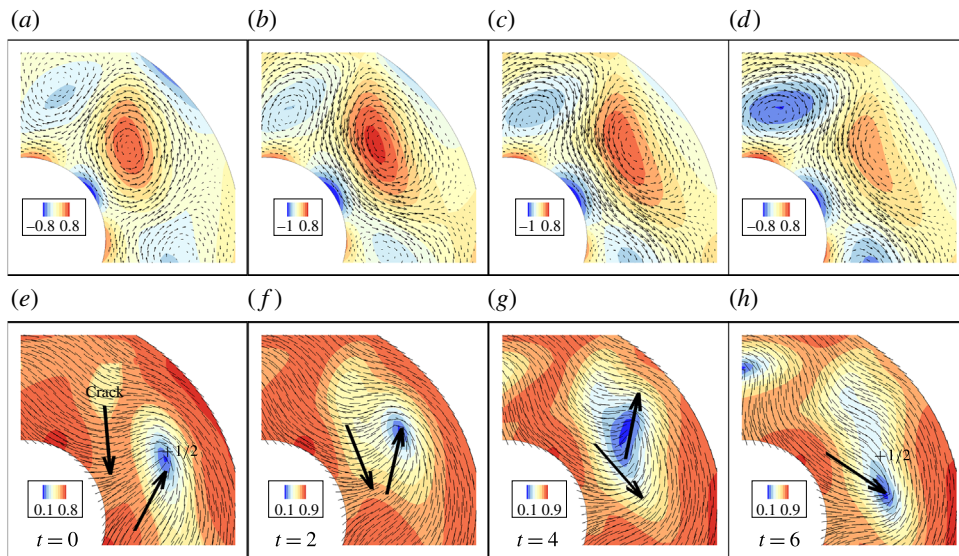
FIGURE 7. (Colour online) (*a–d*) Short-time evolution of the flow (velocity vector overlaid on the colourmap of Ω) and (*e–h*) nematic fields (nematic director overlaid on the colourmap of *s*) for the case shown in figure 6. In (*e–h*), the black arrows show the direction of the crack formation and $+1/2$ defect movement.

the up-moving $+1/2$ defect before it hits the wall. Corresponding to the nematic structure change, the resultant CCW (CW) vorticity is seen to be strengthened (weakened) when the crack and defect interact, and then weakened (strengthened) during their annihilation. We find that such an oscillating state is very robust when choosing R_1 less than 1.5, and the gap width $R_2 - R_1$ between 1.0 and 1.5 (see also movie S2 for the similar dynamics observed in a smaller annulus). As shown in movie S3, more complex defect dynamics and seemingly chaotic flows dominate when $R_2 - R_1 > 2.0$, resembling the active nematic flows observed in an unbounded domain (Gao *et al.* 2015*b*, 2017).

4. Conclusion

In this work, we have studied the nonlinear dynamics and flow patterns of apolar extensor suspensions confined in an annulus geometry through modelling and simulation. The *BQ*-tensor model with the Bingham closure, which was coarse-grained from a mesoscale kinetic model, was used to describe the evolution of the second-moment **D** tensor (Gao *et al.* 2017). The **D** dynamics equation was coupled with the incompressible Navier–Stokes equations, which were solved by using a Galerkin mixed element method at low Reynolds numbers. We have observed active flow generation and spontaneous coherent structures in both dilute and concentrated suspensions. We have gained physical insights into the analytical structure, hydrodynamic instabilities, and characteristic time and length scales under parallel confinement by performing stability analyses for dilute suspensions in a periodic straight channel. In particular, we have shown analytically the long-wave and finite-wavelength nature of the isotropy–circulation and circulation–travelling-wave instabilities respectively. By using similar models and analyses, we will be able

to explore more challenging situations when active fluids are confined in complex geometries at high dimensions.

Acknowledgements

Supplementary movies

Supplementary movies are available at https://doi.org/10.1017/jfm.2017.759.

REFERENCES

ADAMS, D. W. & ERRINGTON, J. 2009 Bacterial cell division: assembly, maintenance and disassembly of the z ring. *Nat. Rev. Microbiol.* **7**, 642–653.

BINGHAM, C. 1974 An antipodally symmetric distribution on the sphere. *Ann. Stat.* **2**, 1201–1225.

BRICARD, A., CAUSSIN, J., DESREUMAUX, N., DAUCHOT, O. & BARTOLO, D. 2013 Emergence of macroscopic directed motion in populations of motile colloids. *Nature* **503**, 95–98.

CHAUBAL, C. & LEAL, L. 1998 A closure approximation for liquid-crystalline polymer models based on parametric density estimation. *J. Rheol.* **42**, 177–201.

DOI, M. & EDWARDS, S. 1988 *The Theory of Polymer Dynamics,* vol. 73. Oxford University Press.

EZHILAN, B. & SAINTILLAN, D. 2015 Transport of a dilute active suspension in pressure-driven channel flow. *J. Fluid Mech.* **777**, 482–522.

EZHILAN, B., SHELLEY, M. & SAINTILLAN, D. 2013 Instabilities and nonlinear dynamics of concentrated active suspensions. *Phys. Fluids* **25**, 070607.

GAO, T., BETTERTON, M., JHANG, A. & SHELLEY, M. 2017 Analytical structure, dynamics, and coarse-graining of a kinetic model of an active fluid. *Phys. Rev. Fluids* **2**, 093302.

GAO, T., BLACKWELL, R., GLASER, M., BETTERTON, M. & SHELLEY, M. 2015*a* Multiscale modeling and simulation of microtubule/motor protein assemblies. *Phys. Rev.* E **92**, 062709.

GAO, T., BLACKWELL, R., GLASER, M., BETTERTON, M. & SHELLEY, M. 2015*b* Multiscale polar theory of microtubule and motor-protein assemblies. *Phys. Rev. Lett.* **114**, 048101.

GAO, T. & HU, H. 2009 Deformation of elastic particles in viscous shear flow. *J. Comput. Phys.* **228**, 2132–2151.

GAO, T. & LI, Z. 2017 Self-driven droplet powered by active nematics. *Phys. Rev. Lett.* **119**, 108002.

DE GENNES, P. G. 1974 *The Physics of Liquid Crystals*. Oxford, Clarendon Press.

GIOMI, L., BOWICK, M., MA, X. & MARCHETTI, M. 2013 Defect annihilation and proliferation in active nematics. *Phys. Rev. Lett.* **110**, 228101.

GIOMI, L., MAHADEVAN, L., CHAKRABORTY, B. & HAGAN, M. F. 2011 Excitable patterns in active nematics. *Phys. Rev. Lett.* **106**, 218101.

GIOMI, L., MAHADEVAN, L., CHAKRABORTY, B. & HAGAN, M. F. 2012 Banding, excitability and chaos in active nematic suspensions. *Nonlinearity* **25**, 2245.

GUILLAMAT, P., IGNÉS-MULLOL, J. & SAGUÉS, F. 2016*a* Control of active liquid crystals with a magnetic field. *Proc. Natl Acad. Sci. USA* **113** (20), 5498–5502.

GUILLAMAT, P., IGNÉS-MULLOL, J., SHANKAR, S., MARCHETTI, M. C. & SAGUÉS, F. 2016*b* Probing the shear viscosity of an active nematic film. *Phys. Rev.* E **94**, 060602.

HENKIN, G., DECAMP, S. J., CHEN, D. T. N., SANCHEZ, T. & DOGIC, Z. 2014 Tunable dynamics of microtubule-based active isotropic gels. *Phil. Trans. R. Soc. Lond.* A **372** (2029), 20140142.

HOHENEGGER, C. & SHELLEY, M. 2011 *Dynamics of Complex Bio-Fluids*. Oxford University Press.

HU, H., ZHU, M. & PATANKAR, N. 2001 Direct numerical simulations of fluid solid systems using the arbitrary Lagrangian Eulerian technique. *J. Comput. Phys.* **169**, 427–462.

JEWELL, E., WANG, W. & MALLOUKL, T. 2016 Catalytically driven assembly of trisegmented metallic nanorods and polystyrene tracer particles. *Soft Matt.* **12**, 2501–2504.

LUSHI, E., WIOLAND, H. & GOLDSTEIN, R. 2014 Fluid flows generated by swimming bacteria drive self-organization in confined fluid suspensions. *Proc. Natl Acad. Sci. USA* **111**, 9733–9738.

MAIER, W. & SAUPE, A. 1958 Eine einfache molekulare Theorie des nematischen kristallinflüssigen Zustandes. *Zeit. Nat. Teil* A **13**, 564–566.

MARCHETTI, M., JOANNY, J., RAMASWAMY, S., LIVERPOOL, T., PROST, J., RAO, M. & SIMHA, R. 2013 Hydrodynamics of soft active matter. *Rev. Mod. Phys.* **85**, 1143–1189.

RAMASWAMY, S. 2010 The mechanics and statistics of active matter. *Ann. Rev. Cond. Matt. Phys.* **1**, 323–345.

RAVNIK, M. & YEOMANS, J. 2013 Confined active nematic flow in cylindrical capillaries. *Phys. Rev. Lett.* **110**, 026001.

SAINTILLAN, D. & SHELLEY, M. 2008 Instabilities, pattern formation, and mixing in active suspensions. *Phys. Fluids* **20**, 123304.

SAINTILLAN, D. & SHELLEY, M. 2013 Active suspensions and their nonlinear models. *C. R. Phys.* **14**, 497–517.

SANCHEZ, T., CHEN, D., DECAMP, S., HEYMANN, M. & DOGIC, Z. 2012 Spontaneous motion in hierarchically assembled active matter. *Nature* **491**, 431–434.

SHELLEY, M. 2016 The dynamics of microtubule/motor-protein assemblies in biology and physics. *Annu. Rev. Fluid Mech.* **48**, 487–506.

SOKOLOV, A., ARANSON, I., KESSLER, J. & GOLDSTEIN, R. 2007 Concentration dependence of the collective dynamics of swimming bacteria. *Phys. Rev. Lett.* **98**, 158102.

THAMPI, S., DOOSTMOHAMMADI, A., GOLESTANIAN, R. & YEOMANS, J. M. 2015 Intrinsic free energy in active nematics. *Europhys. Lett.* **112**, 28004.

THAMPI, S., GOLESTANIAN, R. & YEOMANS, J. 2014 Instabilities and topological defects in active nematics. *Europhys. Lett.* **105**, 18001.

THEILLARD, M., ALONSO-MATILLA, R. & SAINTILLAN, D. 2017 Geometric control of active collective motion. *Soft Matt.* **13**, 363–375.

TSANG, A. C. H. & KANSO, E. 2016 Density shock waves in confined microswimmers. *Phys. Rev. Lett.* **116**, 048101.

VOITURIEZ, R., JOANNY, J. & PROST, J. 2005 Spontaneous flow transition in active polar gels. *Europhys. Lett.* **69**, 404–410.

WIOLAND, H., LUSHI, E. & GOLDSTEIN, R. 2016 Directed collective motion of bacteria under channel confinement. *New J. Phys.* **18**, 075002.

WIOLAND, H., WOODHOUSE, F., DUNKEL, J., KESSLER, J. & GOLDSTEIN, R. 2013 Confinement stabilizes a bacterial suspension into a spiral vortex. *Phys. Rev. Lett.* **110**, 268102.

WOODHOUSE, F. & GOLDSTEIN, R. 2012 Spontaneous circulation of confined active suspensions. *Phys. Rev. Lett.* **109**, 168105.

WU, K.-T., HISHAMUNDA, J. B., CHEN, D. T. N., DECAMP, S. J., CHANG, Y.-W., FERNÁNDEZ-NIEVES, A., FRADEN, S. & DOGIC, Z. 2017 Transition from turbulent to coherent flows in confined three-dimensional active fluids. *Science* **355** (6331), eaal1979.

WYKES, M. D., PALACCI, J., ADACHI, T., RISTROPH, L., ZHONG, X., WARD, M., ZHANG, J. & SHELLEY, M. 2016 Dynamic self-assembly of microscale rotors and swimmers. *Soft Matt.* **12**, 4584–4589.